Research Square

Preprints are preliminary reports that have not undergone peer review.
They should not be considered conclusive, used to inform clinical practice,
or referenced by the media as validated information.

A Direct Dynamical Mass Measurement for a billion-solar-mass Black Hole in the Early Universe

Minghao Yue

yuemh@arizona.edu

Steward Observatory, the University of Arizona

Xiaohui Fan

University of Arizona

Jinyi Yang

the University of Michigan

Feige Wang

University of Michigan

Anna-Christina Eilers

MIT Kavli Institute for Astrophysics and Space Research https://orcid.org/0000-0003-2895-6218

James Nightingale

School of Mathematics, Statistics and Physics, Newcastle University https://orcid.org/0000-0002-8987-7401

Yuzo Ishikawa

MIT Kavli Institute for Space Research https://orcid.org/0000-0001-7572-5231

Jiani Ding

University of Arizona https://orcid.org/0000-0003-4651-8510

Fabian Walter

Max-Planck-Institut für Astronomie https://orcid.org/0000-0003-4793-7880

Ran Wang

Peking University

Ann Zabludoff

University of Arizona https://orcid.org/0000-0001-6047-8469

Article

Keywords: Quasars, Supermassive Black Holes, Gravitational Lensing

Posted Date: November 20th, 2026

DOI: https://doi.org/10.21203/rs.3.rs-11494900/v1

License: This work is licensed under a Creative Commons Attribution 4.0 International License.
Read Full License

Additional Declarations: There is **NO** Competing Interest.

A Direct Dynamical Mass Measurement for a billion-solar-mass Black Hole in the Early Universe

Minghao Yue[1*], Xiaohui Fan[1], Jinyi Yang[2], Feige Wang[2], Anna-Christina Eilers[3], James Nightingale[4], Yuzo Ishikawa[3], Jiani Ding[1], Fabian Walter[5], Ran Wang[6,7], Ann Zabludoff[1]

[1*]Steward Observatory, University of Arizona, 933 N. Cherry Ave., Tucson, 85721, Arizona, USA.
[2]Department of Astronomy, University of Michigan, 1085 S. University Ave., Ann Arbor, 48109, Michigan, USA.
[3]MIT Kavli Institute for Astrophysics and Space Research, 77 Massachusetts Ave., Cambridge, 02139, Massachusetts, USA.
[4]School of Mathematics, Statistics and Physics, Newcastle University, Herschel Building, Newcastle-upon-Tyne, NE1 7RU, UK.
[5]Max-Planck Institute for Astronomy, Königstuhl 17, D-69117 Heidelberg, Germany.
[6]Department of Astronomy, School of Physics, Peking University, Beijing 100871, P. R. China.
[7]Kavli Institute for Astronomy and Astrophysics, Peking University, Beijing 100871, P. R. China.

*Corresponding author(s). E-mail(s): yuemh@arizona.edu;

Abstract

The existence of billion-solar-mass black holes within the first Gyr after the Big Bang challenges models of supermassive black hole (SMBH) formation and growth. However, previous measurements for high-redshift SMBHs rely on scaling relations of broad emission lines of luminous quasars, which are known to suffer from large systematic uncertainties. We present a direct dynamical mass measurement of a billion-solar-mass black hole in a gravitationally lensed quasar at $\boldsymbol{z = 6.5}$. High-resolution Atacama Large Millimeter/submillimeter Array observations reveal a clear rotation-dominated velocity field at the center of the quasar host galaxy. The source-plane resolution is $\boldsymbol{\sim 50}$ pc around the SMBH,

resolving its sphere-of-influence ($\boldsymbol{r_{\rm SOI} \approx 150}$ **pc**). Using a non-parametric rotating thick disk model, we identify a central unresolved point mass (i.e., the SMBH) with $\boldsymbol{\log M_{\rm BH}\ [M_\odot] = 9.07 \pm 0.06}$, which is higher than the single-epoch virial estimate. The dynamical model suggests $\boldsymbol{M_{\rm BH}/M_{\rm dyn} = 7\%}$ and $\boldsymbol{M_{\rm BH}/M_\star \approx 33\%}$ (with a lower limit of $\boldsymbol{M_{\rm BH}/M_\star > 12\%}$), reinforcing the existence of overmassive black holes in the early Universe. Our analysis demonstrates the feasibility of directly measuring the masses of distant SMBHs via galaxy-scale lensing.

Keywords: Quasars, Supermassive Black Holes, Gravitational Lensing

1 Main

The discovery of luminous quasars at $z \gtrsim 7$ indicates the existence of billion-solar-mass black holes (BHs) in the first Gigayear of cosmic history [1–4], requiring efficient channels of heavy seed BH formation and rapid BH growth. The so-called "overmassive black holes" observed in high-redshift quasars and AGN, with ratios between BH masses and host galaxies' stellar masses of $M_{\rm BH}/M_\star \gtrsim 10\%$ [5–9], strongly indicate that SMBHs grow much faster than their host galaxies in the early Universe in those systems.

However, previous studies have relied on the single-epoch virial method to measure SMBH masses, which applies empirical relations to infer BH masses from quasar broad emission lines and continuum luminosity (e.g., Mg II and Hβ) [10, 11]. This method is known to have large systematic uncertainties ($\sim 0.3-0.5$ dex, e.g., [11]). Recent Very Large Telescope Interferometer (VLTI) observations by GRAVITY+ [12] indicate that single-epoch virial SMBH mass measurements might be overestimated by $\gtrsim 0.5$ dex for luminous quasars. Crucially, the large scatter and biases of single-epoch virial estimators can obscure the real growth history of early SMBHs and the redshift evolution of $M_{\rm BH}/M_{\rm host}$ [13]. Benchmarking tests for high-redshift SMBH mass measurement have been lacking, and the physical interpretation of the high SMBH masses measured for $z > 6$ quasars remains uncertain.

Resolved galaxy kinematics offers an accurate and independent benchmark for SMBH mass measurements, which has been widely used for galaxies in the local Universe [14–17]. However, measuring SMBH masses using galaxy kinematics beyond the local Universe is prohibitively challenging. The spheres of influence (SOIs) of SMBHs have typical sizes of $r_{\rm SOI} \lesssim 100$ pc, unresolved under most observing conditions. Several studies have obtained high-resolution ($\sim 0\farcs02$) Atacama Large Millimeter/submillimeter Array (ALMA) observations for $z > 6$ quasars, finding no convincing evidence for SMBHs influencing host galaxy kinematics [18, 19]. Gravitational lensing effects will boost the effective angular resolution, providing a viable method to directly measure high-redshift SMBH masses via resolved host galaxy dynamics. J0439+1634 ($z = 6.52$) is the best target for this experiment: this object is the only gravitationally-lensed quasar at $z > 5$ known so far [20] with high observed luminosity from rest-frame UV to millimeter wavelengths and high lensing magnification. The single-epoch virial

estimators indicate $M_{\rm BH} = 5.25\times10^8 M_\odot$ using the Mg II line and $M_{\rm BH} = 3.82\times10^8 M_\odot$ using the Hβ line, both with systematic errors of $\sim 0.3-0.5$ dex (Method Section 2.2). The optical quasar has a high magnification of $\mu = 37.1$, enhancing the source-plane resolution by about 6× around the SMBH [21].

To this end, we obtained high-resolution ALMA images for J0439+1634 to probe its far-infrared (FIR) continuum and the [C II] 158 μm fine-structure line. The continuum emission was analyzed by [21], focusing on the lensing model and the dust properties of J0439+1634. This paper analyzes the [C II] emission line and the host galaxy kinematics. Figure 1 presents its image-plane [C II] moments, with a beam size of $0\farcs076 \times 0\farcs040$. We perform pixelated lensing reconstruction for the source-plane [C II] emission in each velocity channel, using the lensing model from [21]. The source reconstruction directly fits the uv-space visibility data (Method Section 2.4.1), returning both the surface brightness and the covariance matrix of source-plane pixels. We estimate the source-plane resolution to be ~ 50 pc around the SMBH (Method Section 2.3). The quasar host galaxy clearly exhibits a rotation-dominated velocity field, and the velocity dispersion around the rotation center is about 120 km s^{-1}. Adopting a SMBH mass of $5.25 \times 10^8 M_\odot$ assuming the single-epoch virial mass is correct, the inferred SOI size is $r_{\rm SOI} = \frac{GM_{\rm BH}}{\sigma^2} \approx 150$ pc. Therefore, the SOI is fully resolved thanks to lensing magnification.

To constrain the SMBH mass via galaxy dynamics, we build two distinct dynamical models for J0439+1634 using different parameterizations. For each model, we forward-model the source plane surface brightness map of each velocity channel, then compute the likelihood of the model utilizing the reconstructed source plane cube and the covariance matrix between source plane pixels. In this way, the model likelihood reflects the correlated noise introduced by interferometer beam smearing and lens mapping (Method Section 2.4.2).

We first attempt to fit the reconstructed source-plane [C II] cube using a thin disk model. We consider two components for the rotation curve. The first component, $V_{\rm disk}(r)$, describes the rotation curve without any central unresolved point mass (i.e., with only the host galaxy's potential). In this model, we adopt an arctangent rotation curve, $V_{\rm disk}(r) = V_0(2/\pi)\arctan(r/r_0)$. The second component is the unresolved point mass (e.g., a SMBH), for which we use $V_{\rm point-mass} = \sqrt{GM_{\rm point}/r}$. The total rotation velocity is computed as $V^2(r) = V^2_{\rm disk} + V^2_{\rm point-mass}$, which accounts for both the point mass and the galaxy's enclosed mass within r (Method Section 2.5). We adopt a constant velocity dispersion across the disk.

Figure 2 shows the best-fit thin disk model (see Method for the detailed fitting process). This model captures the overall velocity field with some residuals (with reduced χ^2 of 1.322), likely due to the oversimplification of the model. For comparison, we also fit a no-point-mass model by removing the point mass component. The best-fit no-point-mass model has a reduced χ^2 of 1.382 and a BIC of -477327, and is decisively ruled out by a ΔBIC = 1066 compared to the with-point-mass model. The inferred point mass component has $\log M_{\rm point}\ [M_\odot] = 9.226 \pm 0.021$. We note that the error bar here only reflects the random error from observational noise. The bottom panels of Figure 2 demonstrate why the with-point-mass model is preferred. First, the $p-v$ plot of the no-point-mass model shows less signal at small radii with large velocities

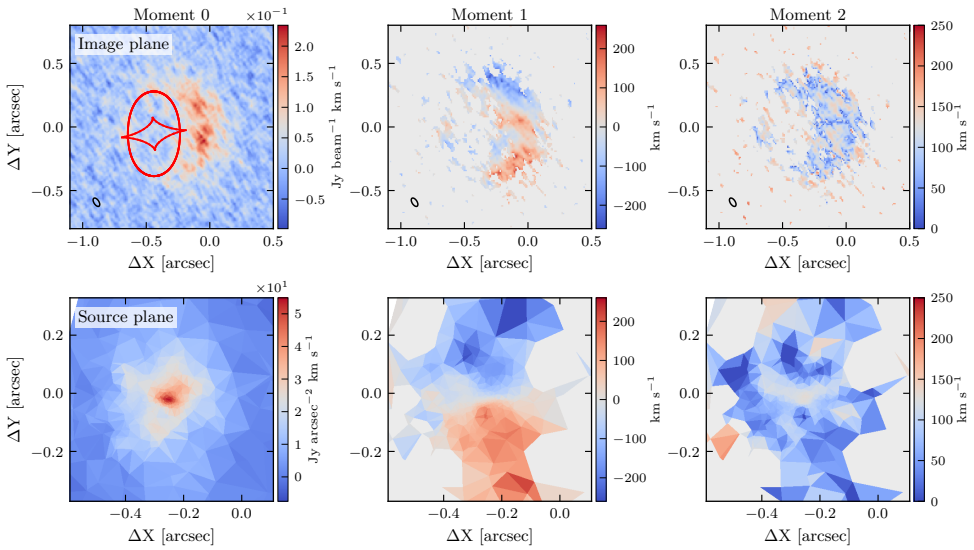

Fig. 1: High-resolution ALMA observation of the [C II] emission of J0439+1634. *Top:* the clean images. From left to right: the velocity-integrated intensity (moment 0), the mean velocity (moment 1), and the velocity dispersion (moment 2). The black circle demonstrates the beam, which has a size of $0\farcs076 \times 0\farcs040$. *Bottom:* the source-plane reconstructed emission. The source reconstruction shows a clear rotation-like velocity field. The velocity dispersion at the center is about 120 km s^{-1}. The estimated SOI radius is $r_{\rm SOI} \approx 150$ pc. The effective source-plane resolution is about 50 pc near the optical quasar [21], and the SOI is well-resolved.

compared to the observation, while a central point mass increases the rotation velocity at small radii and matches observations better. Second, the no-point-mass model gives a narrower spectral width for the central aperture compared to the observation, while a central point mass broadens the central aperture's spectral width due to the Keplerian motion of gas around the point mass (e.g., [19]).

The thin disk model has several oversimplifications that might bias the point mass constraint. First, real galaxies have finite thickness ($\sim 50-100$ pc for $z > 6$ quasars, [18, 22]), comparable to the SMBH's SOI radius. Second, the rotation curve and velocity dispersion profile might not be well-described by simple analytical functions such as arctangent or constant. To mitigate these effects, we build a thick disk model with a non-parametric rotation curve. In this model, we use cubic spline functions to describe both $V(r)$ and $\sigma(r)$, with radial knots at $r = 0, 0\farcs01, 0\farcs02, 0\farcs04, 0\farcs06, 0\farcs08, 0\farcs10, 0\farcs12$. We do not include the point mass term $V_{\rm point-mass}$ in this model; the impact of a potential point mass is described by the radial knots at $r < 0\farcs03$, which sample the expected SOI of the SMBH ($r_{\rm SOI} \approx 150$ pc). For this model, we only fit the $r < 0\farcs1$ region, since the SMBH has negligible influence at larger radii. The detailed modeling procedure and results are described in Method Section 2.5.2.

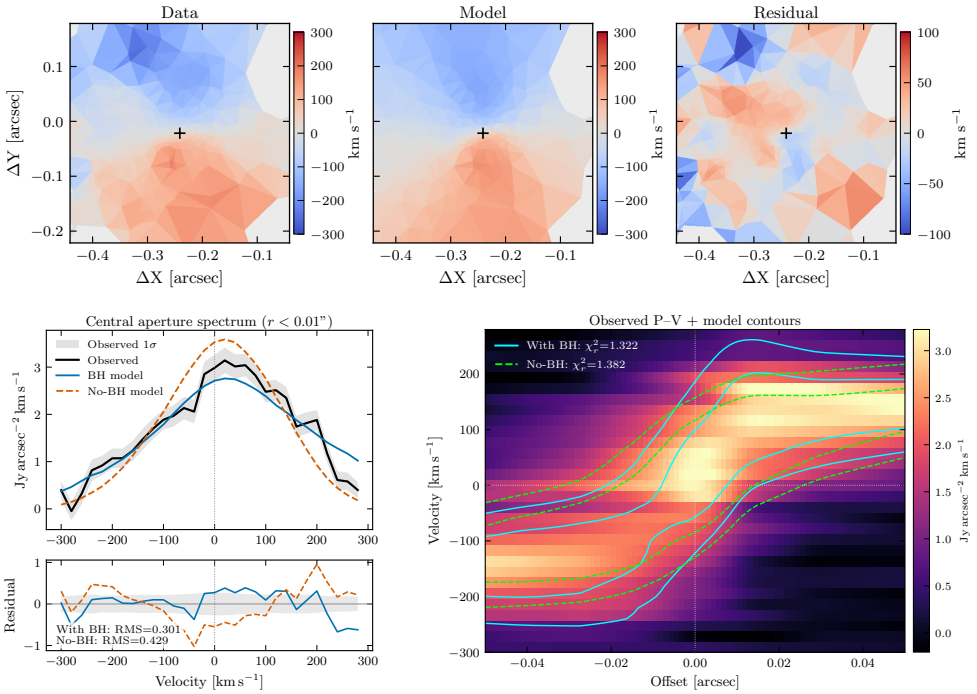

Fig. 2: Thin-disk model with an arctangent rotation curve. *Top:* From left to right, the observed moment-1 map, the model moment-1 map, and the residual map. The model reproduces the main kinematic features of J0439+1634. *Bottom:* Comparison between models with and without a point-mass component. Left: spectrum extracted from the central $r < 0\farcs01$ aperture. Right: position–velocity diagram along the major axis, using a slit width of $0\farcs02$. Solid and dashed contours show the models with and without a point mass, respectively. The point-mass model yields a lower reduced χ^2 and smaller residuals in the central-aperture spectrum than the model without a point mass. We find $\Delta\mathrm{BIC} = 1066$, decisively favoring the point-mass model and implying $\log M_{\mathrm{point}}\ [M_\odot] = 9.226 \pm 0.021$.

Figure 3 demonstrates the result of the spline-rotation-curve thick disk model. The best-fit model has a reduced χ^2 of 1.070, indicating that the model describes the fitted $r < 0\farcs1$ region very well. The model suggests an enclosed mass of $\log M_{\mathrm{enc}}\ [M_\odot] = 9.07 \pm 0.06$ within $0\farcs01$. Since the effective source-plane resolution at $r = 0$ is about $0\farcs01$, we interpret this enclosed mass as a central unresolved massive object. The sharp increase of the best-fit velocity dispersion profile also indicates the existence of a central massive object. This result confirms the presence of an unresolved mass of $> 10^9 M_\odot$ at the center of J0439+1634 revealed by the thin-disk model. Intriguingly, this central unresolved mass naturally emerges even if we do not include a point mass component in the rotation curve.

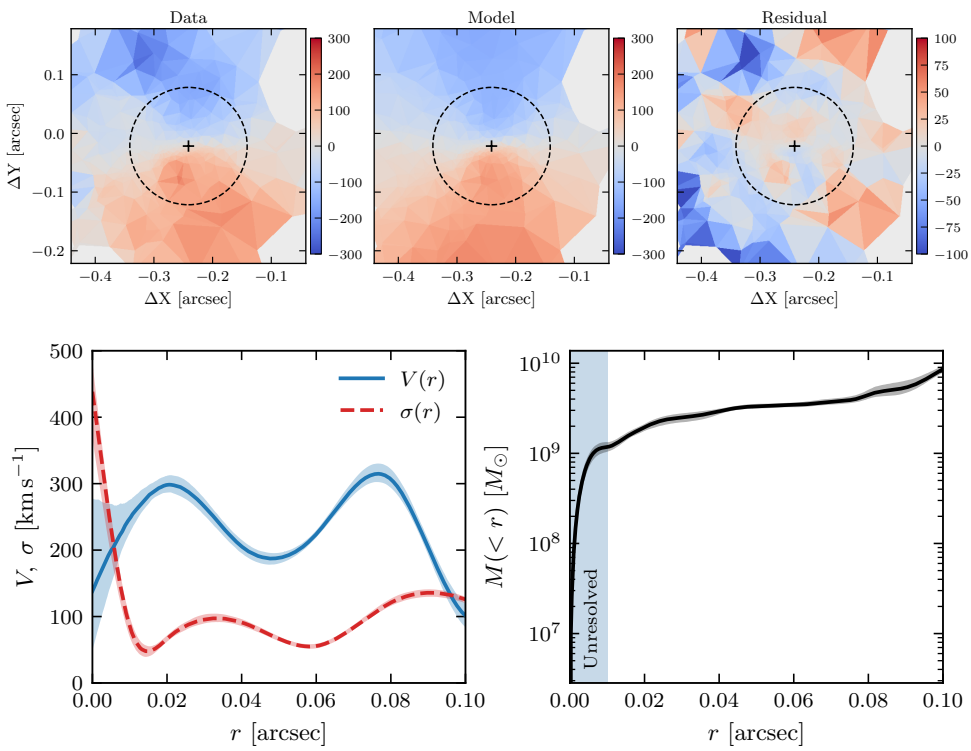

Fig. 3: The thick disk model with a Spline rotation curve and a velocity dispersion profile. *Top:* the observed and modeled source-plane moment 1 maps and their difference. The black dashed circle marks the central $r < 0\farcs1$ region where the fit is performed. The model describes the observation well with $\chi^2_r = 1.070$. *Bottom left:* the posterior distribution of $V(r)$ and $\sigma(r)$. The lines and the shaded regions mark the median and the 1σ confidence region. *Bottom Right:* the enclosed mass. The gray shaded region marks the 1σ confidence region, and the blue shaded region marks the unresolved central aperture. Both the sharp rise of $\sigma(r)$ and the enclosed mass plot indicate an unresolved mass with $M \sim 10^9 M_\odot$.

In Figure 4, we compare the constraints on the central unresolved point mass from the two distinct dynamical models. Both model constraints are consistent within uncertainties, indicating a billion-solar-mass object at J0439+1634's center. We also include the SMBH mass measurement from the single-epoch virial estimator, which has large uncertainties and is $\sim 2-3\times$ lower than the unresolved point mass from host galaxy kinematics. Given the existence of a type-I quasar, the most natural and plausible explanation for the central unresolved point mass in the kinematic models is a SMBH (see Method Section 2.6 for discussions about other less-likely scenarios). Given the better flexibility of the thick disk model, in the following text, we take $\log M_{\rm enc}\ [M_\odot] = 9.07 \pm 0.06$ from that model as the fiducial SMBH mass for J0439+1634.

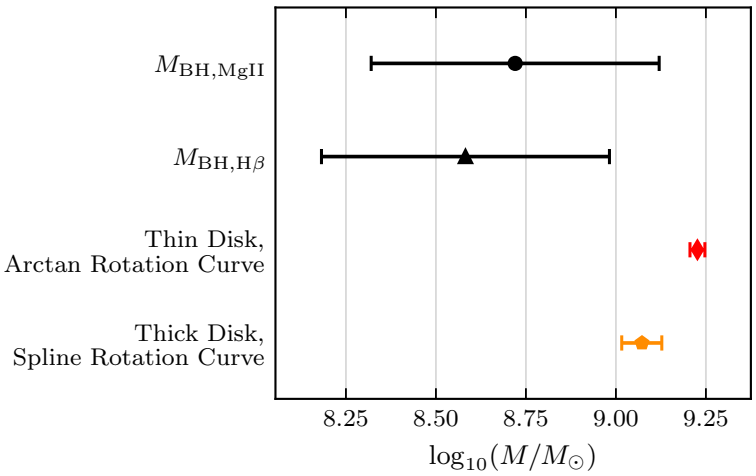

Fig. 4: Comparing different SMBH mass measurements for J0439+1634. The quasar broad line measurements are based on the Mg II and Hβ lines (Section 2.2). The colored points are the measurements from the two different dynamical models in this work. All the models yield consistent results, suggesting the existence of a massive object with $M > 10^9 M_\odot$ at the galaxy's center.

With the host galaxy kinematics model, we estimate that J0439+1634's host galaxy has a dynamical mass of $\log(M_{\rm dyn}/M_\odot) = 10.20 \pm 0.01$ (Method Section 2.5.3). This error bar only reflects the random noise from observations. The BH-to-host mass ratio is 7%, about 2 dex higher than the local $M_{\rm BH} - M_{\rm host}$ relation [23–25]. In Figure 5, we compare J0439+1634 with other $z > 6$ quasars in [26, 27] on the $M_{\rm BH} - M_{\rm dyn}$ plot. With lensing-enhanced source-plane resolution, the $M_{\rm BH}$ and $M_{\rm dyn}$ measurements for J0439+1634 have significantly smaller uncertainties. As this direct SMBH mass measurement is subject to entirely different systematics from single-epoch virial mass measurements, our result independently confirms the high $M_{\rm BH}/M_{\rm dyn}$ ratio of J0439+1634, consistent with the picture where SMBHs in high-redshift luminous quasars obtained their masses earlier than their host galaxies.

Recent James Webb Space Telescope (JWST) observations have found an abundant population of "overmassive BHs" at high redshifts [5, 6, 28–30], although some studies suggested that selection effects (i.e., the Lauer bias, [31]) contribute to the large $M_{\rm BH}/M_{\rm host}$ ratios. Notably, most of these studies use stellar masses ($M_\star$) as the proxy for host galaxy masses. The high $M_{\rm BH}/M_\star$ ratios imply that star formation is slower than SMBH growth in high-redshift AGNs, while some studies argue that the relation between SMBH and its host halo still holds [32]. For example, strong feedback from quasar activity and supernovae can suppress star formation and lead to high $M_{\rm BH}/M_\star$ ratios without significantly altering the relation between SMBHs and their host halo masses. The analysis for J0439+1634 indicates that the SMBH is overmassive even if we count the entire host galaxy's dynamical mass. Therefore, the SMBH

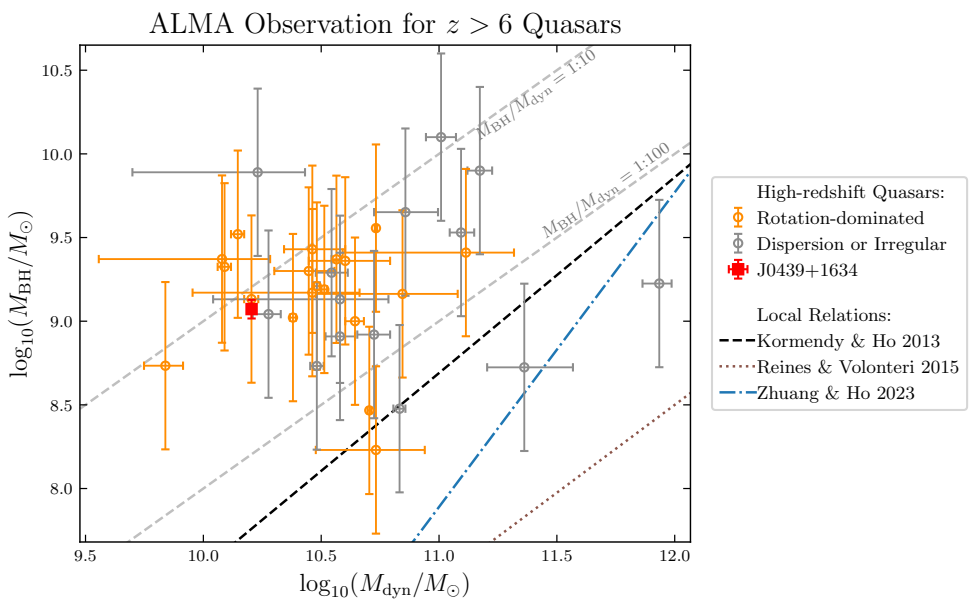

Fig. 5: Position of J0439+1634 on the $M_{\rm BH}$–$M_{\rm dyn}$ diagram. J0439+1634 has $M_{\rm BH}/M_{\rm dyn} = 7\%$, lying ~ 2 dex above the local $M_{\rm BH} - M_{\rm host}$ relations [23–25]. This measurement suggests that the overmassive SMBHs observed in high-redshift quasars cannot be attributed solely to measurement uncertainties. We also compare J0439+1634 with other $z > 6$ quasars that have ALMA-based host-galaxy dynamical-mass estimates [26, 27]. J0439+1634 occupies a region similar to that of other high-redshift quasars.

growth likely precedes the assembly of the entire host galaxy, not only the stellar component, in these systems.

The dynamical mass measurement allows us to constrain the stellar mass of J0439+1634 by mass budgeting. Using far-infrared continuum and the CO(1-0) rotational line, [33, 34] measured the gas and dust masses of J0439+1634, yielding $M_{\rm H_2} = 1.19 \times 10^{10} M_\odot$ and $M_{\rm dust} = 4.9 \times 10^8 M_\odot$. Molecular gas dominates the mass of J0439+1634, consistent with previous studies for $z > 6$ quasars [18, 26, 35]. The room left for the stellar mass is thus $M_\star \lesssim M_{\rm dyn} - M_{\rm H_2} - M_{\rm dust} = 3.6 \times 10^9 M_\odot$. We note that the gas mass estimate in [33, 34] assumes a CO-to-H_2 conversion factor of $\alpha_{\rm CO} = 0.8 M_\odot ({\rm K\ km\ s^{-1} pc^2})^{-1}$; the lowest conversion factor seen for galaxies is about $\alpha_{\rm CO} \approx 0.4 M_\odot ({\rm K\ km\ s^{-1} pc^2})^{-1}$ [36], which gives a lower limit for the gas mass of $M_{\rm H_2} \gtrsim 6 \times 10^9 M_\odot$, and an upper limit of stellar mass of $M_\star \lesssim 9.6 \times 10^9 M_\odot$. Accordingly, we estimate that J0439+1634 has $M_{\rm BH}/M_\star \approx 0.33$, or a lower limit of $M_{\rm BH}/M_\star \gtrsim 0.12$ if we use the stellar mass upper limit. These numbers indicate that J0439+1634 has one of the highest $M_{\rm BH}/M_\star$ ratios seen among high-redshift quasars [28]. Future *JWST*/NIRCam observations might put direct constraints on the stellar mass of J0439+1634.

Our analysis for J0439+1634 demonstrates the feasibility of using galaxy-scale strong lensing for direct SMBH mass measurements. Although recent studies have utilized cluster-scale strong lensing to measure SMBH masses at cosmological distances [30, 37], cluster-scale lenses are much rarer than galaxy-scale lenses. [38] showed that cluster-scale lens contributes only 4% of the total strong-lensing probability, while galaxy-scale lens contributes 84%. Therefore, galaxy-scale lenses provide the best opportunity to build a sample of distant SMBHs with direct mass measurements. Current-generation large sky survey facilities like the Euclid Telescope [39], the Vera C. Rubin Observatory [40] and the Nancy Grace Roman Telescope [41] will find $\gtrsim 100,000$ galaxy-scale lenses [42–44], offering the golden sample for direct SMBH mass measurements. This expected sample will benchmark SMBH mass measurements at all redshifts and provide unprecedented constraints on the SMBH-galaxy coevolution through cosmic time.

2 Method

2.1 Cosmology

We adopt a Flat ΛCDM cosmology with $\Omega_m = 0.3$ and $H_0 = 70$ km s^{-1}Mpc^{-1}.

2.2 Single-Epoch Virial SMBH Mass Estimation for J0439+1634

J0439+1634 was initially reported by [20], who presented the combined optical-to-near-infrared spectrum taken by the Binospec instrument on the 6.5 m MMT telescope, the LRIS instrument on the 10 m Keck I telescope, and the GNIRS instrument on the 8.2 m Gemini-North Telescope. Using the combined spectrum, [20] measures the Mg II broad line width to be $\mathrm{FWHM_{MgII}} = 2924 \pm 188$ km s^{-1}. The estimated SMBH mass, based on the single-epoch virial estimator [45] and assuming no lensing magnification, is $4.93 \times 10^9 M_\odot$. The lensing model in [20] gives $\mu = 51.3$ for the optical quasar, indicating a lensing-corrected SMBH mass of $4.29 \times 10^8 M_\odot$. More recently, [21] updated the lensing model and indicated $\mu = 37.1$ for the optical quasar, inferring a lensing-corrected SMBH mass of $5.25 \times 10^8 M_\odot$. We therefore adopt $M_{\mathrm{BH,MgII}} = 5.25 \times 10^8 M_\odot$ in this work. These SMBH mass estimates have systematic uncertainties of 0.4 dex [45].

J0439+1634 was also observed by JWST NIRSpec/IFU with the F290LP filter and the G395H grating (Program GTO-1222, PI: Willott), which covers the Hβ line and allows us to measure the Hβ-based single-epoch SMBH mass estimate. We obtain the reduced NIRSpec/IFU from [46] and refer the readers to that paper for details about data reduction. We extract the spectrum using an aperture radius of 8 pixels (equivalent to $0\farcs8$). Figure 6 shows the aperture spectrum. We fit the spectrum with a power-law continuum plus Gaussian emission lines, where we use a single Gaussian profile to describe the [O III], an iron line template from [47], and two Gaussian profiles to describe the Hβ line. We assume Gaussian priors for model parameters and use `emcee` [48] to sample the posterior distribution of the parameters. The sampling yields $\mathrm{FWHM_{H\beta}} = 4397^{+2}_{-1}$ km s^{-1} and de-magnified rest-frame 5100Å luminosity

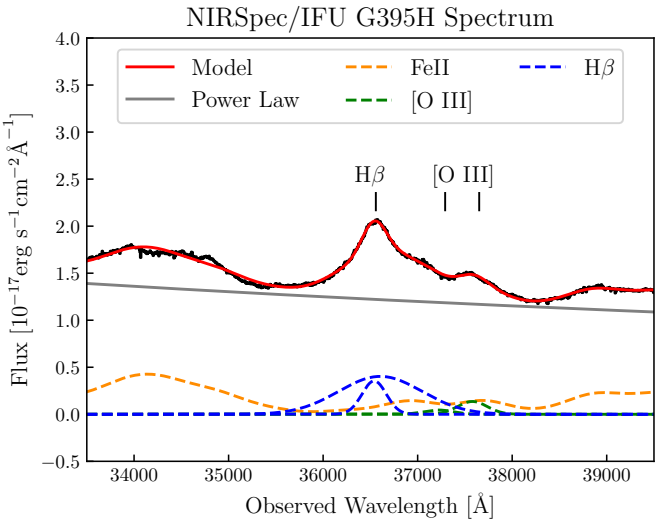

Fig. 6: The NIRSpec/IFU F290LP/G395H spectrum of J0439+1634, showing the wavelengths around the Hβ emission line. The Hβ line has a FWHM of 4397^{+2}_{-1} km s^{-1}, and the de-magnified rest-frame 5100Å luminosity is $\log L_{5100}$[erg s^{-1}] = 44.77291 ± 0.00002. The derived SMBH mass is $M_{\rm BH,H\beta} = 3.82 \times 10^8 M_\odot$ using the relation in [11].

$\log L_{5100}$[erg s^{-1}] = 44.77291 ± 0.00002. We then use the scaling relation in [11] and get $M_{\rm BH,H\beta} = 3.82 \times 10^8 M_\odot$, with the error dominated by the systematic uncertainty of 0.4 dex.

2.3 ALMA Observation and Data Reduction

J0439+1634 was observed by ALMA with program ID 2018.1.00566.S (PI: Fan). Details about these observations and data reduction have been presented in [21], which are briefly described here.

The observations contain two configurations: the C43-5 observation that probes the large-scale ($\sim 1''$) emission of the quasar host galaxy and is crucial for measuring the total flux, and the C43-8 observation that probes the small-scale structures of the emission. The C43-5 observation was taken in 2018 with a total on-source time of 99 minutes. The C43-8 observations were taken in 2019 and 2021 with a total on-source time of 337 minutes. For both configurations, we use four spectral windows (SPWs) to sample the FIR continuum and the [C II] emission line, which have central frequencies of 238.593 GHz, 236.718 GHz, 252.206 GHz, and 253.894 GHz, respectively. All the SPWs have widths of 1.875 GHz.

We reduce the data using CASA [49] version 6.5.4.9. We first combine all the C43-5 and C43-8 observations into one measurement set, then obtain the continuum visibility by splitting out line-free channels using task `split`. Here we define line-free channels as channels with observed frequency $\nu_{\rm obs} < 252.4$ GHz or $\nu_{\rm obs} > 253.1$ GHz [34]. We then run `uvcontsub` to fit the line-free channel continuum with `fitorder`= 1,

then subtract the fitted continuum from the line channels. We then regrid the [C II] line visibilities to a velocity grid covering -300 km s^{-1} to 300 km s^{-1} with a channel width of 20 km s^{-1}, where we set the velocity center at 252.7744 GHz. We run task `tclean` to get the surface brightness map of each channel, using a Briggs weighting with robust = 2. We then run task `immoments` to yield the image-plane moment maps. The resulting moment maps are shown in Figure 1. The image-plane beam size is $0\farcs076 \times 0\farcs040$. Accordingly, we estimate the source-plane resolution around the SMBH to be $\sqrt{0\farcs076 \times 0\farcs040/37.1} = 0\farcs009$, corresponding to about 50 pc at $z = 6.52$.

2.4 Reconstructing the Source-plane [C II] Emission

We adopt the lens model from [21] to reconstruct the source-plane [C II] emission. This model was derived from the ALMA continuum emission, which has a much higher signal-to-noise ratio (S/N= 47 per beam at the peak) than the integrated [C II] emission (S/N= 11 per beam at the peak) and is therefore better suited for lens modeling. The fiducial model consists of a singular isothermal ellipsoid (SIE) lens galaxy and external shear. We note that more flexible lens models, including those with a power-law density profile instead of an SIE, yield lensing parameters consistent with the fiducial SIE model and do not improve the goodness of fit. Further details of the lens modeling are provided in [21].

2.4.1 Pixelated Lensing Reconstruction

We use `PyAutoLens` [50–52] to perform pixelized lens reconstructions of the [C II] emission in each velocity channel. The idea of pixelated lensing reconstruction and its application to interferometer observations have been described in, e.g., [53–57]. Here we briefly describe the idea of pixelated reconstruction, and refer readers to the above-listed papers for more details.

Given the observed visibility data $\vec{d}$ and its covariance matrix $\mathbf{\Sigma}_d$, we can compute the source-plane reconstructed source as

$$\vec{s} = \mathbf{A}^{-1}(\mathbf{DL})^\intercal \mathbf{\Sigma}_d^{-1} \vec{d} \tag{1}$$

[e.g., 55, 57, 58]. Here $\mathbf{L}$ is the lensing operator that maps source-plane emissions to the image plane, and $\mathbf{D}$ represents the effect of the interferometer (including the primary beam and the Fourier transform). The matrix $\mathbf{A}$ is defined as $\mathbf{A} = (\mathbf{DL})^\intercal \mathbf{\Sigma}_d^{-1} (\mathbf{DL}) + \lambda \mathbf{R}^\intercal \mathbf{R}$, where $\mathbf{R}$ is the regularization matrix that punishes source models with large small-scale variations. The regularization matrix prevents the source-plane model from fitting observational noise.

The uncertainty of the reconstructed source can be computed as

$$\mathbf{\Sigma}_s = \mathbf{A}^{-1}(\mathbf{DL})^\intercal \mathbf{\Sigma}_d^{-1} (\mathbf{DL}) \mathbf{A}^{-1} \tag{2}$$

In our case, $\mathbf{L}$ is determined by the continuum-based lensing model. We use the image-plane grid as used in [21], which is an irregular grid adapted to the continuum brightness map, such that the number density of image-plane points is proportional to the continuum surface brightness (see [21] for details). For the regularization matrix $\mathbf{R}$, we use `PyAutoLens`'s constant split regularization. The only free parameter is thus

the regularization strength λ, and we fit its posterior using the nested sampling code `nautilus` [59]. Finally, we take the best-fit λ value and evaluate the source plane surface brightness and uncertainties accordingly.

Figure 7 shows the pixelated lensing reconstruction for all 30 velocity channels. There are no noticeable features in the residual maps, indicating a good fit for these channels. Using the reconstructed sources in these channels, we compute the source-plane moment maps, which are shown in Figure 1. The uncertainties of the reconstructed emissions in each channel are dominated by random noise from observations, as the high S/N of the continuum emission gives a highly-accurate lensing model.

In addition to the pixelated lensing reconstruction for each channel, we also fit the velocity-integrated [C II] visibility (over -300 km s^{-1} to 300 km s^{-1}) using a Sérsic profile. The goal is to measure the Sérsic index n and the half-light radius r_e of the [C II] emission. The fitting yields $n = 0.94 \pm 0.02$ and $r_e = 0\farcs209 \pm 0\farcs003$, i.e., a nearly-exponential disk with a half-light radius of 1.14 ± 0.02 kpc. These numbers are close to the low-resolution-only ALMA observation ($n = 0.82 \pm 0.05$ and $r_e = 0\farcs233 \pm 0\farcs006$; [34]).

2.4.2 Source-plane Pixel Correlation with Strong Lensing

One non-trivial aspect in the analysis is the source-plane beam smearing effect. Strong gravitational lensing maps a single source-plane pixel to multiple image-plane pixels, and the interferometer observation further produces correlations between image-plane pixels. Consequently, there is no well-defined source-plane beam, and the correlation between reconstructed source-plane pixels is heterogeneous.

To correctly evaluate the model likelihood and sample the posterior distributions of the model parameters, we forward-model both the visibility measurement and the source-plane reconstruction for each source-plane model. Specifically, for a source-plane model $\vec{s_m}$, the forward-modeled visibility $\vec{d_m}$ is

$$\vec{d_m} = \mathbf{DL}\vec{s_m} \tag{3}$$

Then, forward-modeling the pixelated reconstruction for $\vec{d_m}$ yields reconstructed source plane emission $\vec{s'_m}$ corresponding to $\vec{s_m}$:

$$\vec{s'_m} = \mathbf{A}^{-1}(\mathbf{DL})^\intercal \mathbf{\Sigma}_d^{-1} \vec{d_m} = \mathbf{A}^{-1}(\mathbf{DL})^\intercal \mathbf{\Sigma}_d^{-1} \mathbf{DL}\vec{s_m} \tag{4}$$

This vector $\vec{s'_m}$ can be directly compared to the source plane reconstruction $\vec{s}$ from Equation 1. Specifically, when fitting a disk model (Section 2.5), we first build the raw source-plane map $\vec{s_m}$ free of lensing and interferometer effects, then compute the reconstructed source-plane map $\vec{s'_m}$ using Equation 4. We then compute the log-likelihood of the model via

$$\log L = -0.5 \times \left(\vec{s'_m} - \vec{s}\right)^\intercal \mathbf{\Sigma}_s^{-1} \left(\vec{s'_m} - \vec{s}\right) \tag{5}$$

We use Equation 5 to evaluate the posterior distributions of model parameters. For fitting with masked region, we only count unmasked pixels in $\vec{s}$, $\vec{s'_m}$, and $\mathbf{\Sigma}_s$.

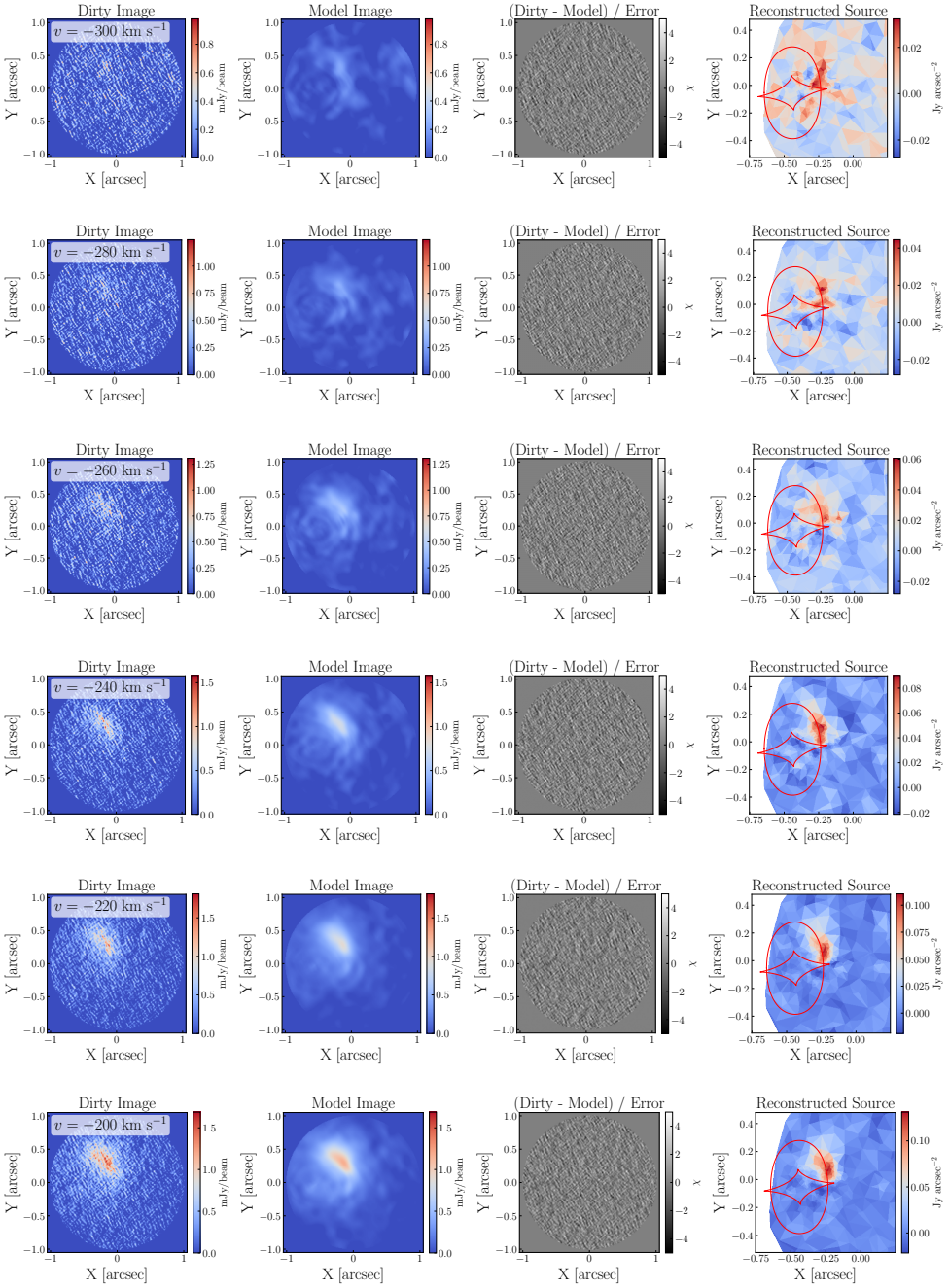

Fig. 7: The reconstructed [C II] source for each velocity channel. From left to right: the observed dirty map, the modeled dirty map, the residual, the source-plane reconstruction. The red lines mark the lensing caustics.

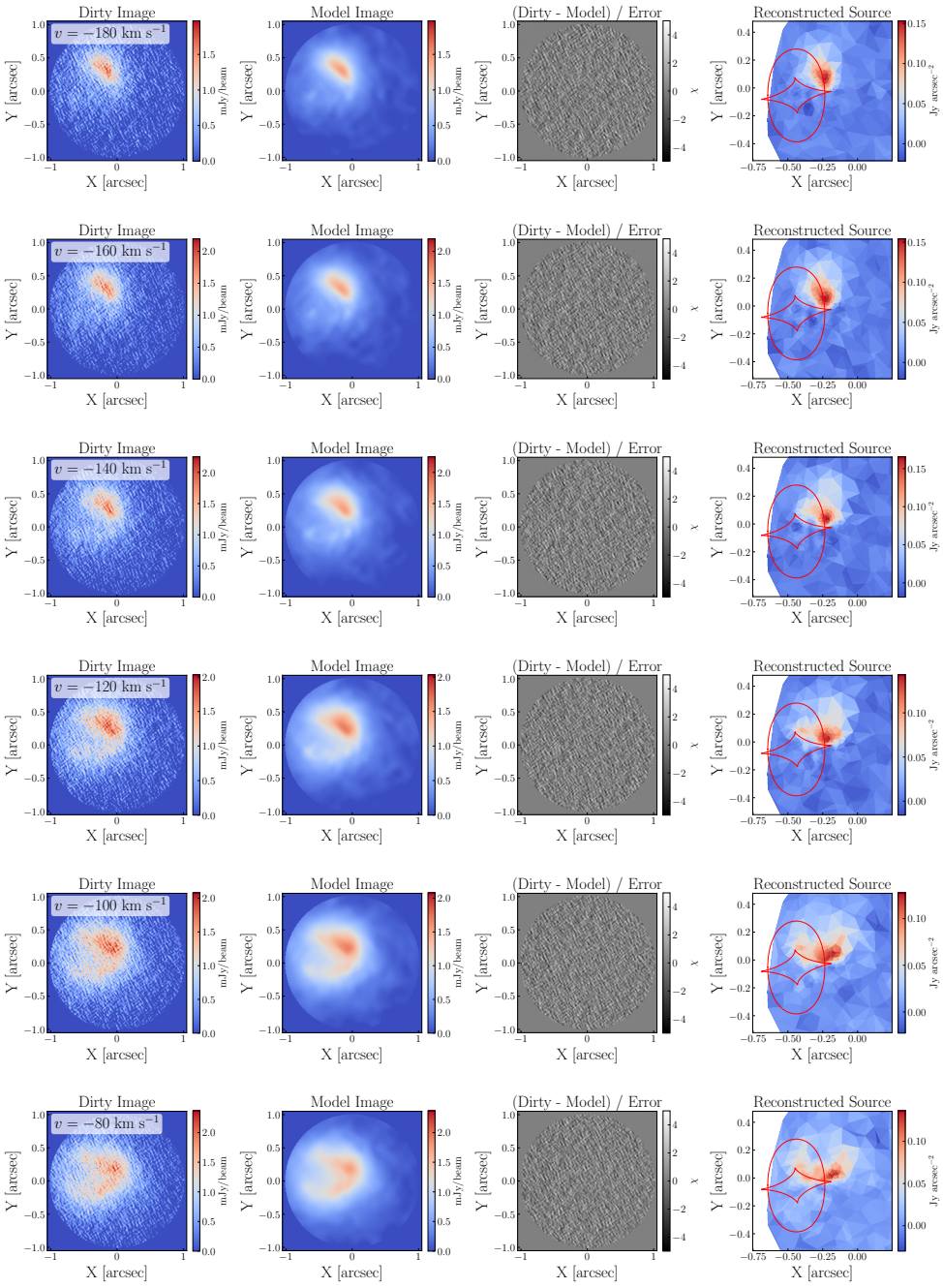

Fig. 7: Continued.

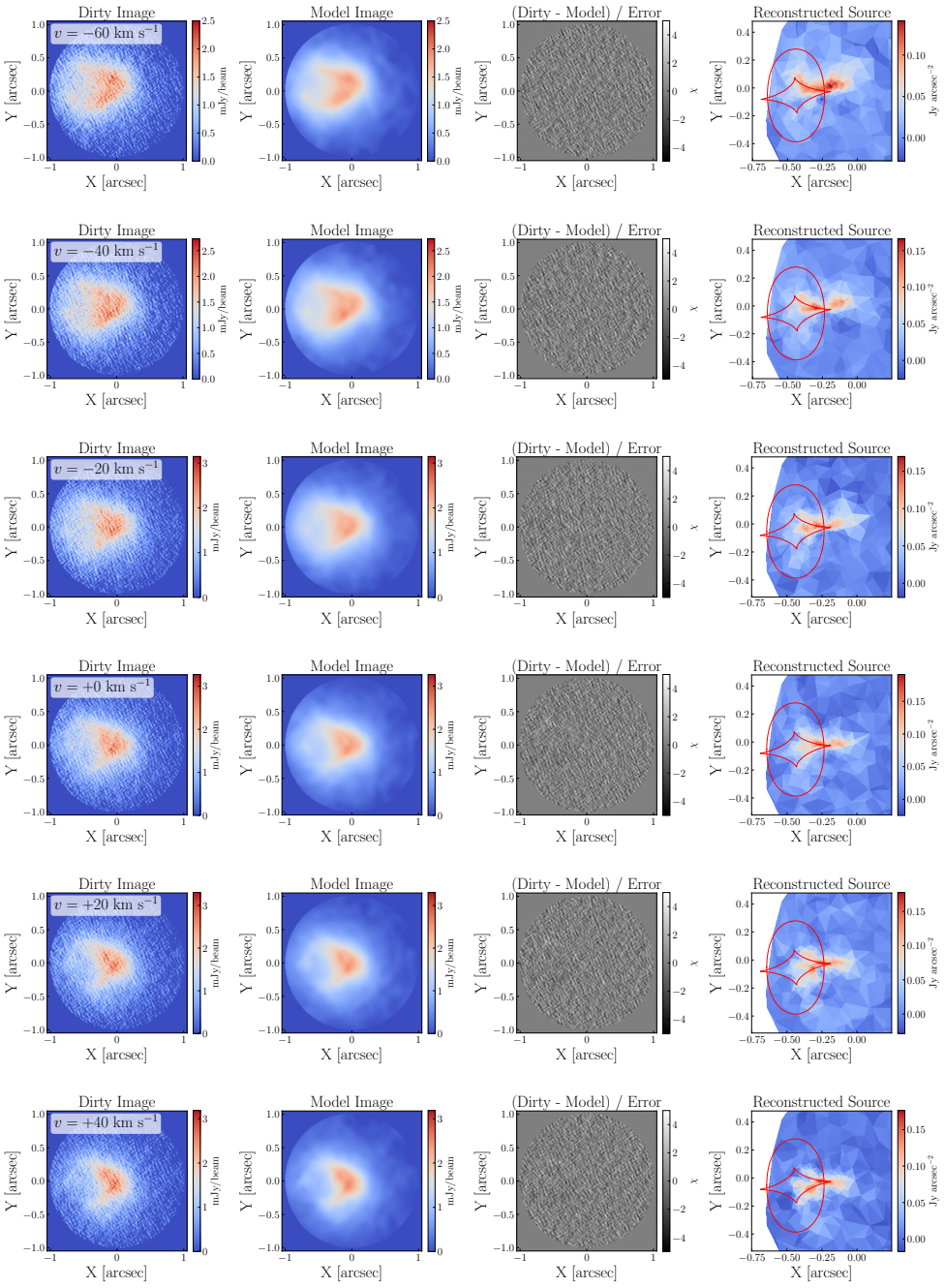

Fig. 7: Continued.

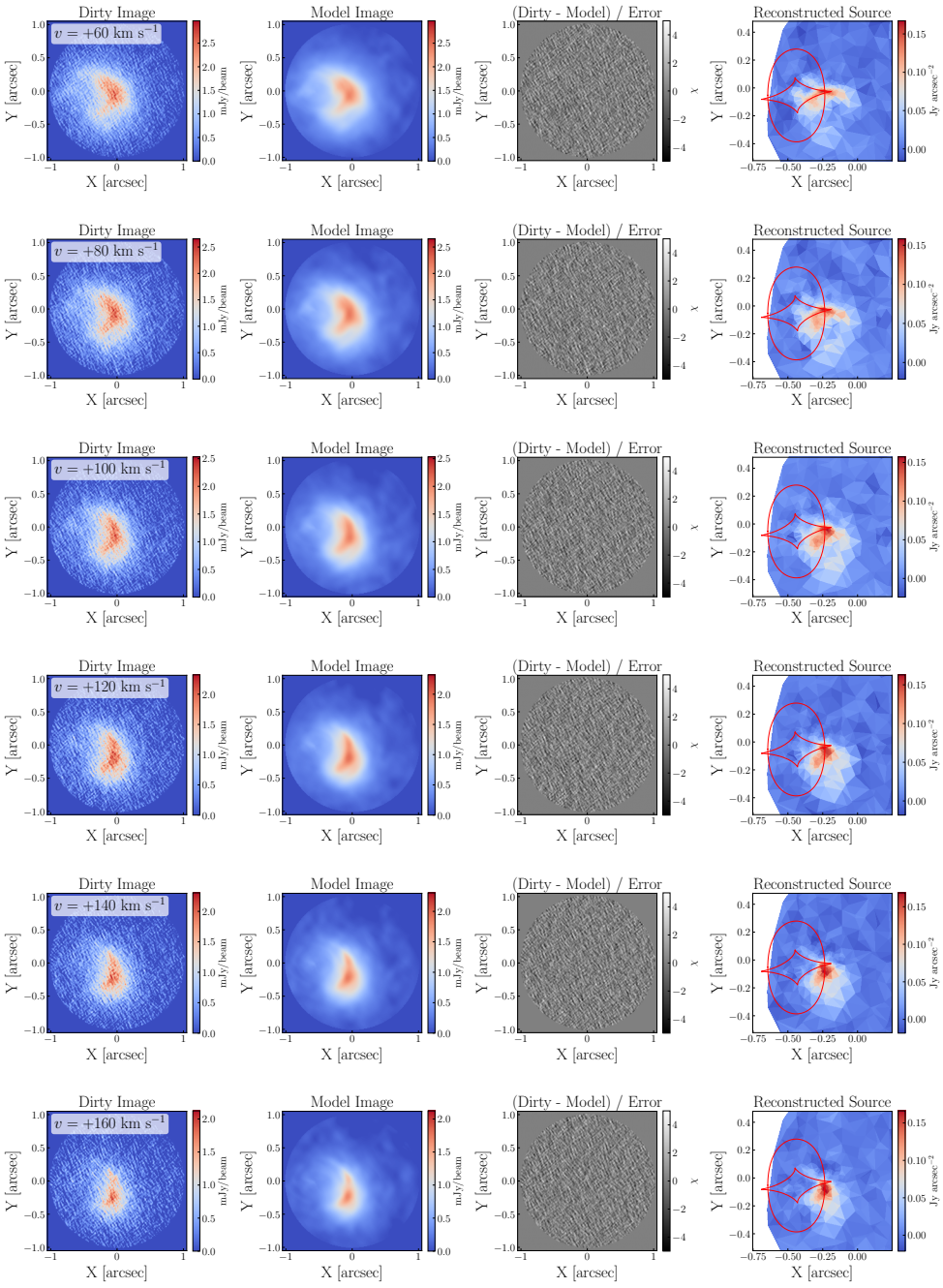

Fig. 7: Continued.

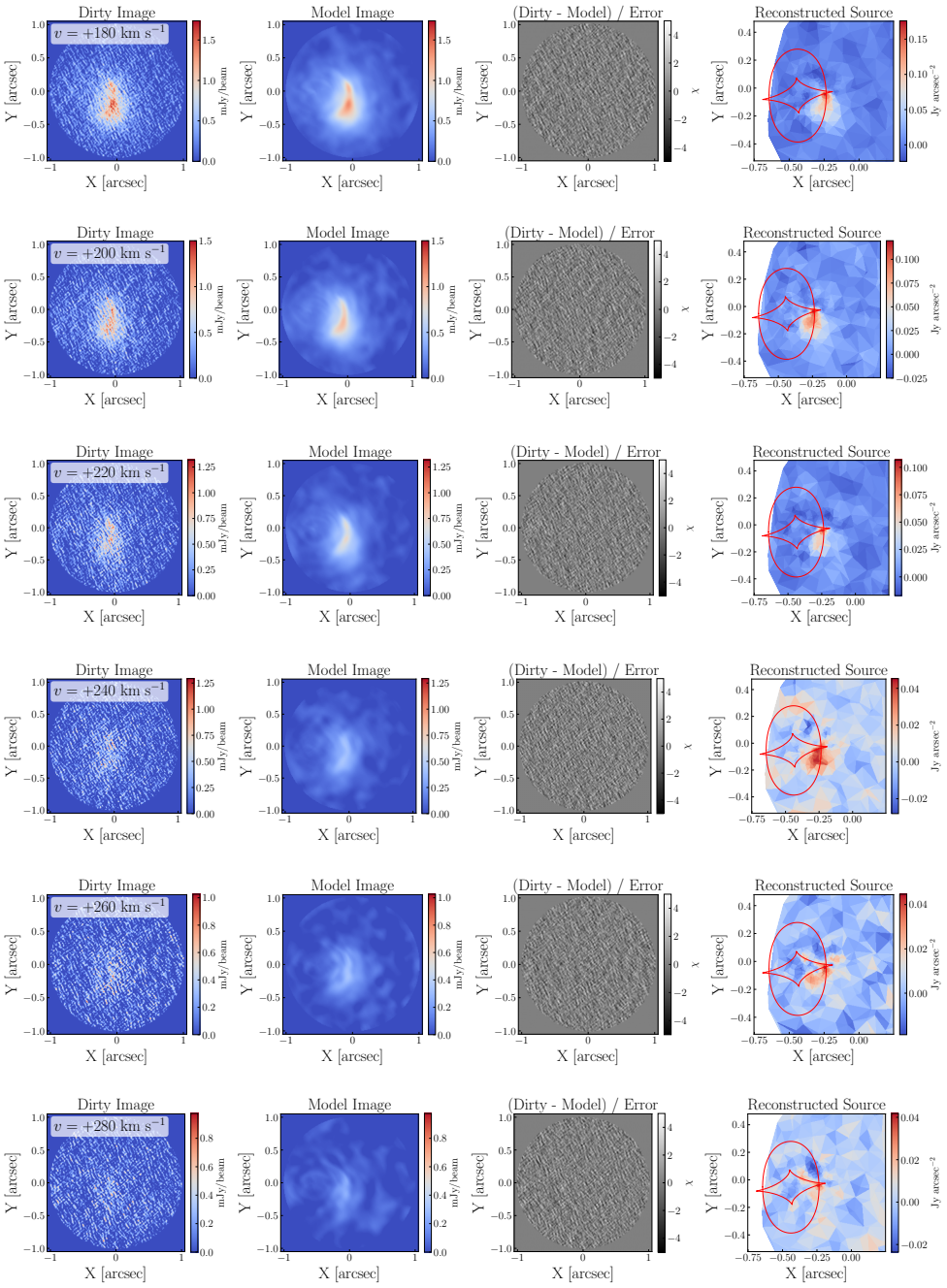

Fig. 7: Continued.

2.5 Rotating Disk Models

2.5.1 Thin Disk Model with Arctan-rotation-curve

The first model we explore is a thin disk with an arctan-form rotation curve and a constant velocity dispersion profile for the host galaxy. This model has been widely used in studies of high-redshift rotating galaxies [60, 61]. Specifically, the rotation curve is described as

$$V^2(r) = V_{\rm disk}^2 + \frac{GM_{\rm point}}{r} = \left[\frac{2}{\pi} V_0 \arctan\left(\frac{r}{r_0}\right)\right]^2 + \frac{GM_{\rm point}}{r} \tag{6}$$

Here $V_{\rm disk}(r)$ is the rotation curve of the host galaxy without a central point mass (e.g., the SMBH), and the $GM_{\rm point}/r$ term accounts for the impact of the central point mass. This parameterization allows us to isolate the impact of the SMBH from the host galaxy's potential. We assume a constant velocity dispersion σ_0 across the disk.

We use customized code to model the [C II] emission map in each velocity channel. We do not use publicly available packages like `qubefit` [61] or `kinMS` [62], as these packages cannot model the complicated source-plane beam smearing in the case of strong lensing. In this work, we follow the algorithm of 3DBarolo [63] to produce the raw source emission, then compute the reconstructed source following the algorithm described in Section 2.4.2. Specifically, we set up a rectangular grid on the source plane and project the source-plane pixels onto the thin disk's plane, using the inclination i and position angle ϕ of the disk. We compute the galactocentric radius of each pixel and assign a circular rotation velocity according to the rotation curve (Equation 6). The rotation velocity is then projected along the line of sight to obtain $v_{\rm los}$. Each pixel is assigned a Gaussian line profile with mean velocity $v_{\rm los}$ and intrinsic velocity dispersion σ_0. The integrated flux of each pixel is set by the Sérsic profile fit described in Section 2.4.1. Finally, we normalize the total flux for each pixel such that the reconstructed moment-0 map matches the observed moment-0 map.

We validate our code by comparing the modeled unconvolved source emission to the output of 3DBarolo. We emphasize that the final normalization step is both critical and standard in galaxy kinematic modeling: by fixing the spatial flux distribution, it prevents irregular surface-brightness structure from biasing the inferred kinematic parameters. As a result, the specific flux profile adopted to initialize the model cube (i.e., the Sérsic profile) does not affect the final kinematic fit.

The thin disk model has seven free parameters, namely the disk inclination i, the position angle ϕ, the max rotation velocity V_0, the turnover radius r_0, the velocity dispersion σ_0, the central velocity $V_{\rm cen}$, and the SMBH mass $M_{\rm point}$. We fix the center of the disk to the continuum peak where the SMBH is located [21]. We run `nautilus` to obtain the posterior distributions of these parameters. We assume flat priors for all parameters, except for $M_{\rm point}$, which has a log-flat prior. For the no-point-mass comparison model, we fix $M_{\rm point} = 0$. The information and the posterior distributions of these parameters are listed in Table 1.

Table 1: The parameters of the arctangent rotation curve thin disk model

Parameter	Prior	Posterior
Inclination, i (degrees)	flat at [0,90]	$48.97^{+0.77}_{-0.79}$
Position angle, ϕ (degrees)	flat at [-180,180]	$-82.56^{+0.23}_{-0.23}$
Central velocity, $V_{\rm cen}$ (km s^{-1})	flat at [-100,100]	$-6.31^{+0.30}_{-0.30}$
Maximum velocity, V_0 (km s^{-1})	flat at [0,700]	$178.3^{+2.1}_{-2.0}$
Turnover radius, r_0 ($''$)	flat at $[0.001, 0.5]$	$0.00179^{+0.00094}_{-0.00057}$
Velocity dispersion, σ_0 (km s^{-1})	flat at $[0, 300]$	$84.50^{+0.39}_{-0.40}$
Central point mass, $\log M_{\rm point}$ $[M_\odot]$	flat at $[6, 10]$	$9.226^{+0.021}_{-0.021}$

Note. The posterior values and uncertainties correspond to the 50th, 16th, and 84th percentiles of the posterior distribution. The disk center is fixed to the continuum peak reported in [21].

2.5.2 Thick Disk Model with Non-parametric Rotation Curve and Velocity Dispersion Profile

The thin disk model has several obvious oversimplifications. First, real galaxies have finite thickness ($\sim 10^2$ pc, [18, 22]) comparable to the SMBH's sphere-of-influence radius. Second, the rotation curve and velocity dispersion profile might not be well-described by simple analytical functions like arctan or constant. To test whether the point mass signal in the thin disk model is biased by these assumptions, we explore a thick disk model with a non-parametric rotation curve and velocity dispersion profile.

Specifically, we set radial knots $r = 0, 0\farcs01, 0\farcs02, 0\farcs04, 0\farcs06, 0\farcs08, 0\farcs10, 0\farcs12$, and allow $V(r_j)$ and $\sigma(r_j)$ to vary freely. We then obtain the full $V(r)$ and $\sigma(r)$ curves using cubic spline interpolation. The dense sampling at $r < 0\farcs03$ captures the rise of V or σ at small radii caused by a possible central massive object. We further set a constraint that the enclosed galaxy mass should be monotonically increasing with r. Following [64], we compute the enclosed mass as

$$\frac{GM(<r)}{r} = V^2(r) - r\sigma^2(r)\frac{\partial \ln[\rho(r)\sigma^2(r)]}{\partial r} \tag{7}$$

where $\rho(r)$ is the density of the rotating gas. We use the Sérsic parameters derived in Section 2.4.1 to yield $\rho(r) = \rho_0 \exp\{-b_n\left[(r/r_e)^{1/n} - 1\right]\}$. Note that the normalization ρ_0 cancels in the partial derivative, and only r_e and n matter in Equation 7.

We follow the algorithm of 3Dbarolo to model the emission of the thick disk. We first establish a three-dimensional grid in the thick disk's cylindrical coordinate system, then compute the rotation velocity and velocity dispersion for each cell. The brightness of each cell I is computed based on the Sérsic profile parameters and the scale height z_0, where we assume $I(z) \propto \exp(-z/z_0)$. Each disk-frame cell is projected to its sky position and deposited onto the source-plane grid by cloud-in-cell (i.e., bilinear) interpolation, distributing its flux among the four nearest pixels with weights given by the fractional pixel offsets. Finally, we normalize the total intensity of each source-plane pixel so that the modeled source-plane moment 0 matches the observed

one. Again, we validate our customized code by comparing the modeled unconvolved cube to the output of 3DBarolo.

The thick disk model has 20 parameters, including the inclination i, the position angle ϕ, the central velocity $V_{\rm cen}$, the scale height z_0, eight rotation velocities, and eight velocity dispersions at the radial knots. We first attempt to fit this model with all parameters free, but the resulting inclination converges to 0, meaning that the model is too flexible to constrain the inclination. Therefore, we fix the inclination to the median posterior value from the thin disk model, $i = 48.97°$. When computing the likelihood, we only account for the central $r < 0\farcs1$ region, as the central point mass has negligible impact on the outskirt region. We perform the fitting using `Nautilus` and adopt flat priors for all parameters. The fitting result is presented in Table 2.

Table 2: The parameters of the thick disk model with Spline rotation curve and velocity dispersion profile

Parameter	Prior	Posterior
Position angle, ϕ (degrees)	[-180, 180]	$-88.36^{+0.41}_{-0.46}$
Disk scale height, z_0 ($''$)	[0.001, 0.1]	$0.0037^{+0.0025}_{-0.0017}$
Central velocity, $V_{\rm cen}$ (km s^{-1})	[-100, 100]	$4.18^{+0.79}_{-0.79}$
Rotation velocity at $r = 0$ (km s^{-1})	[0, 1000]	153^{+139}_{-103}
Rotation velocity at $r = 0\farcs01$ (km s^{-1})	[0, 1000]	248^{+29}_{-23}
Rotation velocity at $r = 0\farcs02$ (km s^{-1})	[0, 1000]	297^{+13}_{-11}
Rotation velocity at $r = 0\farcs04$ (km s^{-1})	[0, 1000]	206^{+10}_{-11}
Rotation velocity at $r = 0\farcs06$ (km s^{-1})	[0, 1000]	$224.4^{+5.9}_{-5.5}$
Rotation velocity at $r = 0\farcs08$ (km s^{-1})	[0, 1000]	307^{+14}_{-13}
Rotation velocity at $r = 0\farcs10$ (km s^{-1})	[0, 1000]	102^{+18}_{-19}
Rotation velocity at $r = 0\farcs12$ (km s^{-1})	[0, 1000]	$226.6^{+4.6}_{-4.6}$
Velocity dispersion at $r = 0$ (km s^{-1})	[0, 500]	437^{+42}_{-71}
Velocity dispersion at $r = 0\farcs01$ (km s^{-1})	[0, 500]	86^{+13}_{-15}
Velocity dispersion at $r = 0\farcs02$ (km s^{-1})	[0, 500]	$66.6^{+5.0}_{-4.7}$
Velocity dispersion at $r = 0\farcs04$ (km s^{-1})	[0, 500]	$90.8^{+5.5}_{-5.3}$
Velocity dispersion at $r = 0\farcs06$ (km s^{-1})	[0, 500]	$55.8^{+3.5}_{-3.5}$
Velocity dispersion at $r = 0\farcs08$ (km s^{-1})	[0, 500]	$121.1^{+5.6}_{-5.3}$
Velocity dispersion at $r = 0\farcs10$ (km s^{-1})	[0, 500]	$125.3^{+4.6}_{-4.9}$
Velocity dispersion at $r = 0\farcs12$ (km s^{-1})	[0, 500]	$63.3^{+1.8}_{-1.7}$

Note. The posterior values and uncertainties correspond to the 50th, 16th, and 84th percentiles of the posterior distribution. The disk center is fixed to the continuum peak reported in [21]. The disk inclination is fixed to the median value from the arctan-rotation-curve thin disk fit (Table 1).

2.5.3 Dynamical Mass and Mass Budget of the Host Galaxy

Following [26], we measure the dynamical mass of J0439+1634 within $r < 2r_e$. To ensure a fair comparison with previous studies of quasar host galaxies, we estimate $M_{\rm dyn}$ using the same thin-disk model with an arctan rotation curve. We use Equation

7 to compute the dynamical mass. Using the posterior distribution of the model parameters, we derive $M_{\rm dyn} = (1.60 \pm 0.04) \times 10^{10} M_\odot$. This result is consistent with the measurement in [34], who gives $M_{\rm dyn} \sin^2(i) = 7.9 \times 10^9 M_\odot$ using low-resolution ALMA observations.

2.6 Implication of the Unresolved Point Mass

The most natural explanation for the billion-solar-mass unresolved point mass is an SMBH, given the existence of the optical type-I quasar. In this Section, we discuss another plausible scenario for central compact mass components in galaxies, namely nuclear star clusters (NSCs).

NSCs have a typical mass range of $10^5 M_\odot$ to $10^8 M_\odot$, and the most massive NSCs reach about $10^9 M_\odot$ [65]. If the unresolved mass in J0439+1634 is an NSC, it will be one of the most massive NSCs known to date. NSCs with $M \sim 10^9 M_\odot$ have sizes $r \sim 50 - 100$ pc [66], marginally consistent with the source-plane beam size around the galaxy center (~ 50 pc). Nevertheless, we consider the NSC scenarios extremely unlikely for the following reasons. First, massive NSCs ($M > 10^8 M_\odot$) have extended star formation histories, typically spanning several Gyrs [67], whereas the age of the Universe is only ~ 800 Myrs at J0439+1634's redshift. Second, the masses of NSCs correlate with those of their host galaxies; [66] shows that, at the massive end, the relation is

$$\log(M_{\rm NSC}/M_\odot) = 0.92 \log(M_\star/10^9 M_\odot) + 6.13 \quad (8)$$

with an intrinsic scatter of 0.18 dex. By taking a conservative upper limit of $M_\star < M_{\rm dyn} = 1.6 \times 10^{10} M_\odot$, we yield $\log(M_{\rm NSC}/M_\odot) = 7.24 \pm 0.18$ for J0439+1634, far smaller the unresolved massive object. Therefore, the NSC scenario is essentially ruled out for J0439+1634, leaving a SMBH the most natural and plausible scenario for the unresolved massive object.

Artificial Intelligence Disclosure

We use Large Language Models to aid the coding in this study, including GPT-6 Astra [68], Claude Opus 5, Opus 5.5, Fable 5, and Fable 5.1 [69]. We also use these tools to improve the writing of the manuscript.

Acknowledgements. M.Y. thanks the support from the Steward Observatory, the University of Arizona via the Bart J. Bok Fellowship.

- Funding
  This study is supported by the Steward Observatory, the University of Arizona via the Bart J. Bok Fellowship.
- Conflict of interest/Competing interests
  The authors declare no competing interests.
- Ethics approval and consent to participate
- Consent for publication
- Data availability

The ALMA observations for J0439+1634 are available at https://almascience.nrao.edu/aq/.

- Materials availability
- Code availability

  CASA is publicly available at https://casa.nrao.edu/.
- Author contribution

  X.F., J.Y., F.W., and M.Y. conceived the project idea. M.Y. performed the data reduction and analysis. M.Y. led the interpretation of the results, and the other authors provided comments about the result interpretation and paper writing.

References

[1] Bañados, E. *et al.* An 800-million-solar-mass black hole in a significantly neutral Universe at a redshift of 7.5. *Nat* **553**, 473–476 (2018).

[2] Yang, J. *et al.* Pōniuā'ena: A Luminous z = 7.5 Quasar Hosting a 1.5 Billion Solar Mass Black Hole. *ApJ* **897**, L14 (2020).

[3] Wang, F. *et al.* A Luminous Quasar at Redshift 7.642. *ApJ* **907**, L1 (2021).

[4] Yang, D. *et al.* Euclid: Discovery of 31 new quasars at 6.6 ¡ z ¡ 7.8. *A&A* **711**, A104 (2026).

[5] Pacucci, F., Nguyen, B., Carniani, S., Maiolino, R. & Fan, X. JWST CEERS and JADES Active Galaxies at z = 4-7 Violate the Local M $_{\bullet}$-M $_{\star}$ Relation at ¿3σ: Implications for Low-mass Black Holes and Seeding Models. *ApJ* **957**, L3 (2023).

[6] Yue, M. *et al.* EIGER. V. Characterizing the Host Galaxies of Luminous Quasars at z $\gtrsim$ 6. *ApJ* **966**, 176 (2024).

[7] Stone, M. A., Lyu, J., Rieke, G. H., Alberts, S. & Hainline, K. N. Undermassive Host Galaxies of Five z $\sim$ 6 Luminous Quasars Detected with JWST. *ApJ* **964**, 90 (2024).

[8] Durodola, E., Pacucci, F. & Hickox, R. C. Exploring the Active Galactic Nucleus Fraction of a Sample of JWST's Little Red Dots at 4 ¡ z ¡ 8: Overmassive Black Holes Are Strongly Favored. *ApJ* **985**, 169 (2025).

[9] Meyer, R. A. *et al.* Life After the Quasar: Overmassive Black Holes and Remnant Ionised Bubbles in and Around Two z~6.6 Galaxies. *arXiv e-prints* arXiv:2605.00763 (2026).

[10] Greene, J. E. & Ho, L. C. Estimating Black Hole Masses in Active Galaxies Using the Hα Emission Line. *ApJ* **630**, 122–129 (2005).

[11] Vestergaard, M. & Peterson, B. M. Determining Central Black Hole Masses in Distant Active Galaxies and Quasars. II. Improved Optical and UV Scaling

Relationships. *ApJ* **641**, 689–709 (2006).

[12] Abuter, R. *et al.* A dynamical measure of the black hole mass in a quasar 11 billion years ago. *Nat* **627**, 281–285 (2024).

[13] Li, J. *et al.* Tip of the Iceberg: Overmassive Black Holes at 4 ¡ z ¡ 7 Found by JWST Are Not Inconsistent with the Local Relation. *ApJ* **981**, 19 (2025).

[14] Barth, A. J. *et al.* Measurement of the Black Hole Mass in NGC 1332 from ALMA Observations at 0.044 arcsecond Resolution. *ApJ* **822**, L28 (2016).

[15] Ruffa, I. *et al.* WISDOM project - XIV. SMBH mass in the early-type galaxies NGC 0612, NGC 1574, and NGC 4261 from CO dynamical modelling. *MNRAS* **522**, 6170–6195 (2023).

[16] Zhang, H. *et al.* WISDOM Project - XXV. Improving the CO-dynamical supermassive black hole mass measurement in the galaxy NGC 1574 using high spatial resolution ALMA observations. *MNRAS* **541**, 2540–2552 (2025).

[17] Zhang, H. *et al.* WISDOM Project - XXII. A 5 per cent precision CO-dynamical supermassive black hole mass measurement in the galaxy NGC 383. *MNRAS* **537**, 520–536 (2025).

[18] Walter, F. *et al.* ALMA 200 pc Imaging of a z 7 Quasar Reveals a Compact, Disk-like Host Galaxy. *ApJ* **927**, 21 (2022).

[19] Meyer, R. A., Neeleman, M., Walter, F. & Venemans, B. ALMA 300 pc Resolution Imaging of a z = 6.79 Quasar: No Evidence for Supermassive Black Hole Influence on the C II Kinematics. *ApJ* **956**, 127 (2023).

[20] Fan, X. *et al.* The Discovery of a Gravitationally Lensed Quasar at z = 6.51. *ApJ* **870**, L11 (2019).

[21] Yue, M. *et al.* High-Resolution ALMA Imaging for a Gravitationally-lensed Quasar at $z = 6.5$: Constraining the AGN Contribution to Galactic-Scale Dust Heating. *arXiv e-prints* arXiv:2606.11084 (2026).

[22] Neeleman, M. *et al.* ALMA 400 pc Imaging of a z = 6.5 Massive Warped Disk Galaxy. *ApJ* **958**, 132 (2023).

[23] Kormendy, J. & Ho, L. C. Coevolution (Or Not) of Supermassive Black Holes and Host Galaxies. *ARA&A* **51**, 511–653 (2013).

[24] Reines, A. E. & Volonteri, M. Relations between Central Black Hole Mass and Total Galaxy Stellar Mass in the Local Universe. *ApJ* **813**, 82 (2015).

[25] Zhuang, M.-Y. & Ho, L. C. Evolutionary paths of active galactic nuclei and their host galaxies. *Nature Astronomy* **7**, 1376–1389 (2023).

[26] Neeleman, M. *et al.* The Kinematics of z $\gtrsim$ 6 Quasar Host Galaxies. *ApJ* **911**, 141 (2021).

[27] Wang, F. *et al.* A Spatially Resolved [C II] Survey of 31 z $\sim$ 7 Massive Galaxies Hosting Luminous Quasars. *ApJ* **968**, 9 (2024).

[28] Marshall, M. A. *et al.* GA-NIFS and EIGER: A merging quasar host at z = 7 with an overmassive black hole. *A&A* **702**, A50 (2025).

[29] Tripodi, R. *et al.* Extreme properties of a compact and massive accreting black hole host in the first 500 Myr. *Nature Communications* **16**, 9830 (2025).

[30] Juodžbalis, I. *et al.* A direct black-hole mass measurement in a little red dot at high redshift. *Nat* **653**, 1017–1021 (2026).

[31] Lauer, T. R., Tremaine, S., Richstone, D. & Faber, S. M. Selection Bias in Observing the Cosmological Evolution of the $M_\bullet$-σ and $M_\bullet$-L Relationships. *ApJ* **670**, 249–260 (2007).

[32] Liu, W. *et al.* A $z \sim 6.2$ Quasar on the Local M_{BH}-σ_* Relation Quenching Its Host Galaxy from the Aether Survey. *arXiv e-prints* arXiv:2606.03037 (2026).

[33] Yang, J. *et al.* Far-infrared Properties of the Bright, Gravitationally Lensed Quasar J0439+1634 at z = 6.5. *ApJ* **880**, 153 (2019).

[34] Yue, M. *et al.* ALMA Observations of the Sub-kpc Structure of the Host Galaxy of a z = 6.5 Lensed Quasar: A Rotationally Supported Hyper-Starburst System at the Epoch of Reionization. *ApJ* **917**, 99 (2021).

[35] Kaasinen, M. *et al.* The cold molecular gas in z $\gtrsim$ 6 quasar host galaxies. *A&A* **684**, A33 (2024).

[36] Narayanan, D., Krumholz, M. R., Ostriker, E. C. & Hernquist, L. A general model for the co–h2 conversion factor in galaxies with applications to the star formation law. *Monthly Notices of the Royal Astronomical Society* **421**, 3127–3146 (2012). URL https://doi.org/10.1111/j.1365-2966.2012.20536.x.

[37] Newman, A. B. *et al.* A stellar dynamical mass measurement of an inactive black hole at redshift 2. *arXiv e-prints* arXiv:2503.17478 (2025).

[38] Oguri, M. The image separation distribution of strong lenses: halo versus subhalo populations. *MNRAS* **367**, 1241–1250 (2006).

[39] Euclid Collaboration *et al.* Euclid: I. Overview of the Euclid mission. *A&A* **697**, A1 (2025).

[40] Ivezić, Ž. *et al.* LSST: From Science Drivers to Reference Design and Anticipated Data Products. *ApJ* **873**, 111 (2019).

[41] Akeson, R. *et al.* The Wide Field Infrared Survey Telescope: 100 Hubbles for the 2020s. *arXiv e-prints* arXiv:1902.05569 (2019).

[42] Collett, T. E. The Population of Galaxy-Galaxy Strong Lenses in Forthcoming Optical Imaging Surveys. *ApJ* **811**, 20 (2015).

[43] Weiner, C., Serjeant, S. & Sedgwick, C. Predictions for Strong-lens Detections with the Nancy Grace Roman Space Telescope. *Research Notes of the American Astronomical Society* **4**, 190 (2020).

[44] Wedig, B. *et al.* The Roman View of Strong Gravitational Lenses. *ApJ* **986**, 42 (2025).

[45] McLure, R. J. & Dunlop, J. S. The cosmological evolution of quasar black hole masses. *MNRAS* **352**, 1390–1404 (2004).

[46] Leung, G. C. K. *et al.* Discovery of quasar variability and early accretion disk signatures at cosmic dawn. *Nature Astronomy* (2026).

[47] Park, D., Barth, A. J., Ho, L. C. & Laor, A. A New Iron Emission Template for Active Galactic Nuclei. I. Optical Template for the Hβ Region. *ApJS* **258**, 38 (2022).

[48] Foreman-Mackey, D., Hogg, D. W., Lang, D. & Goodman, J. emcee: The MCMC Hammer. *PASP* **125**, 306 (2013).

[49] CASA Team *et al.* CASA, the Common Astronomy Software Applications for Radio Astronomy. *PASP* **134**, 114501 (2022).

[50] Nightingale, J. W. *et al.* 'pyautolens': Open-source strong gravitational lensing. *J. Open Source Softw.* **6**, 2825 (2021). URL https://doi.org/10.21105/joss.02825.

[51] Nightingale, J. W. & Dye, S. Adaptive semi-linear inversion of strong gravitational lens imaging. *MNRAS* **452**, 2940–2959 (2015).

[52] Nightingale, J. W., Dye, S. & Massey, R. J. AutoLens: Automated modeling of a strong lens's light, mass, and source. *MNRAS* **478**, 4738–4784 (2018). URL https://academic.oup.com/mnras/article/478/4/4738/5001434.

[53] Warren, S. J. & Dye, S. Semilinear Gravitational Lens Inversion. *ApJ* **590**, 673–682 (2003).

[54] Suyu, S. H., Marshall, P. J., Hobson, M. P. & Blandford, R. D. A Bayesian analysis of regularized source inversions in gravitational lensing. *MNRAS* **371**, 983–998 (2006).

[55] Hezaveh, Y. D. *et al.* Detection of Lensing Substructure Using ALMA Observations of the Dusty Galaxy SDP.81. *ApJ* **823**, 37 (2016).

[56] Litke, K. C. *et al.* Spatially Resolved [C II] Emission in SPT0346-52: A Hyper-starburst Galaxy Merger at z $\sim$ 5.7. *ApJ* **870**, 80 (2019).

[57] Maresca, J. & Dye, S. The impact of CLEANing on strong gravitational lens modelling. *MNRAS* **537**, 2708–2725 (2025).

[58] Powell, D. *et al.* A novel approach to visibility-space modelling of interferometric gravitational lens observations at high angular resolution. *MNRAS* **501**, 515–530 (2021).

[59] Lange, J. U. nautilus: boosting Bayesian importance nested sampling with deep learning. *Monthly Notices of the Royal Astronomical Society* **525**, 3181–3194 (2023). URL https://doi.org/10.1093/mnras/stad2441.

[60] Neeleman, M., Prochaska, J. X., Kanekar, N. & Rafelski, M. A cold, massive, rotating disk galaxy 1.5 billion years after the Big Bang. *Nat* **581**, 269–272 (2020).

[61] Neeleman, M., Prochaska, J. X., Kanekar, N. & Rafelski, M. qubefit: MCMC kinematic modeling. Astrophysics Source Code Library, record ascl:2005.013 (2020). 2005.013.

[62] Davis, T. A., Zabel, N. & Dawson, J. M. KinMS: Three-dimensional kinematic modeling of arbitrary gas distributions. Astrophysics Source Code Library, record ascl:2006.003 (2020). 2006.003.

[63] Di Teodoro, E. M. & Fraternali, F. ^{3D} BAROLO: a new 3D algorithm to derive rotation curves of galaxies. *MNRAS* **451**, 3021–3033 (2015).

[64] Iorio, G. *et al.* LITTLE THINGS in 3D: robust determination of the circular velocity of dwarf irregular galaxies. *MNRAS* **466**, 4159–4192 (2017).

[65] Georgiev, I. Y., Böker, T., Leigh, N., Lützgendorf, N. & Neumayer, N. Masses and scaling relations for nuclear star clusters, and their co-existence with central black holes. *MNRAS* **457**, 2122–2138 (2016).

[66] Neumayer, N., Seth, A. & Böker, T. Nuclear star clusters. *A&A Rev.* **28**, 4 (2020).

[67] Fahrion, K. *et al.* Diversity of nuclear star cluster formation mechanisms revealed by their star formation histories. *A&A* **650**, A137 (2021).

[68] OpenAI. ChatGPT 5.6 Sol. https://chatgpt.com/ (2026).

[69] Anthropic. Claude Opus 5. https://claude.ai/ (2026).